SUPPLEMENTARY INFORMATION

Reconfigurable Terahertz Optoelectronic Logic through Charge-Density-Wave Phase Engineering

Xin Sun[1,2†], Kening Xiao[3†], Yingdong Wei[1,4†], Wenqi Mo[3], Libo Zhang[3*], Shijian Tian[1], Xiaokai Pan[1], Yage Yang[1], Shiqi Lan[1], Yichong Zhang[1], Zhen Hu[1], Kaixuan Zhang[3], Li Han[5], Fang Wang[1*], Xiaoshuang Chen[1,2,3,4], Lin Wang[1*], Weida Hu[1,3*]

[1]State Key Laboratory for Infrared Physics, Shanghai Institute of Technical Physics, Chinese Academy of Sciences, 500 Yu-tian Road, Shanghai 200083, China.

[2]School of Microelectronics Shanghai University, 20 Chengzhong Road, Shanghai 201899, China.

[3]College of Physics and Optoelectronic Engineering, Hangzhou Institute for Advanced Study, University of Chinese Academy of Sciences, No. 1, Sub-Lane Xiangshan, Xihu District, Hangzhou 310024, China.

[4]School of Physical Science and Technology, ShanghaiTech University, Shanghai 201210, China.

[5]College of Optical and Electronic Technology, China Jiliang University, Hangzhou 310018, China;

†: These authors contributed equally: Xin Sun, Kening Xiao, Yingdong Wei

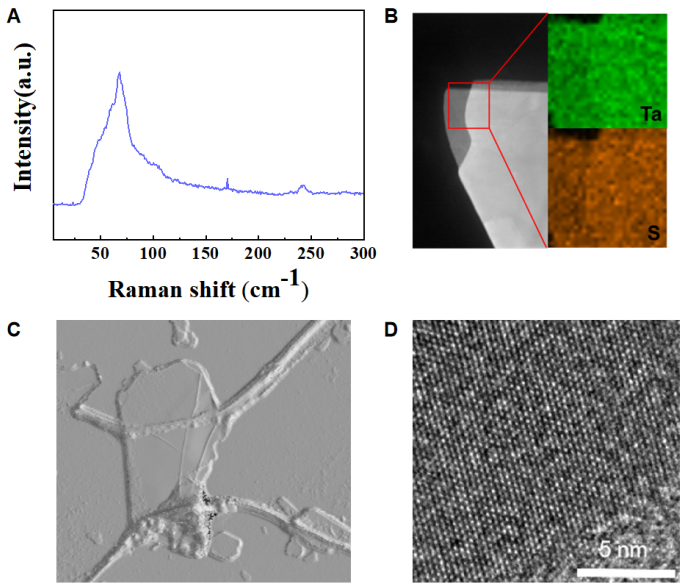

Figure S1. **Material Structure and Characterization Diagrams.** (A) Raman spectroscopy on 1T-TaS_2. Figure S1A shows a Raman spectroscopy measurement of the 1T-TaS_2 sample. The spectrum displays a prominent peak at approximately 70 cm^{-1}, which corresponds to the characteristic A_{1g} phonon mode of 1T-TaS_2 in its charge density wave phase. The peak arises from the out-of-plane vibrations of Ta atoms within the David-star clusters. (B) The elemental mapping results from energy-dispersive X-ray spectroscopy (EDX) or electron energy loss spectroscopy (EELS). The grayscale optical/SEM image on the left shows the overall morphology of the flake, while the false-colored images on the right display the spatial distribution of tantalum (Ta, green) and sulfur (S, orange) elements. The uniform distribution of both elements confirms the stoichiometric composition and high crystalline quality of the exfoliated 1T-TaS_2 flake, with the expected Ta ratio of approximately 1:2. (C) Electron image of surface morphology. The micrograph reveals several flake-like structures with sharp, well-defined edges typical of mechanically exfoliated transition metal dichalcogenides. The contrast variations across the surface suggest thickness differences between different

regions. The surface appears largely free from contamination or oxide formation, indicating successful preservation of material quality through the h-BN encapsulation process described in our fabrication method. (D) TEM image of 1T-TaS_2. Figure S1D shows a high-resolution transmission electron microscopy (HRTEM) image with atomic resolution. The hexagonal lattice pattern is clearly visible, confirming the crystalline structure of 1T-TaS_2. The scale bar indicates 5 nm, allowing observation of the atomic arrangement with excellent resolution. The periodic lattice exhibits the expected hexagonal symmetry with no visible defects or discontinuities, indicating high structural quality of the material. The uniform contrast across the image suggests consistent thickness and crystalline ordering throughout the sample area.

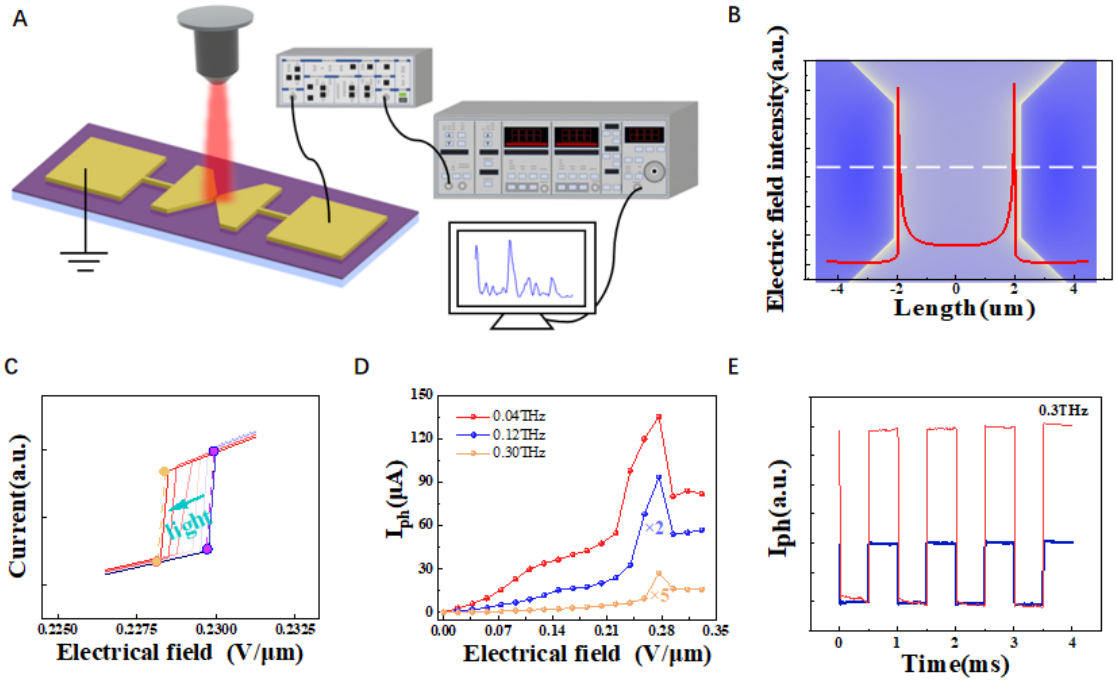

Figure S2. **THz Detection Performance of 1T-TaS_2 Device.** (A) The test process diagram of the PD. By constructing a terahertz photoelectric signal testing and characterization system, direct detection of terahertz photoelectric signals has been achieved. The system consists of the microwave source (Agilent E8257D), the preamplifier (SR570), the lock-in amplifier (SR830), frequency multiplier, and the computer control system based on LabVIEW. We connect the microwave signal output from the microwave source to the frequency multiplier to obtain terahertz light, then connect the device to the preamplifier, which amplifies the photocurrent signal into a voltage signal. This signal is then fed into the lock-in amplifier, and after processing, it is connected to the computer control system to record the optical response. After calculating the link loss, the magnitude of the photocurrent is finally obtained. (B) FDTD modeling of the butterfly antenna structure, simulating the electric field distribution at 0.3 THz. By using the finite-difference in time domain method to model

the butterfly antenna with a channel length of 4 μm. The incident beam is a polarized plane wave which polarization direction is parallel to the channel. It can be seen that the antenna coupling to the terahertz light effectively enhances the electric field distribution at the interface between the channel and the metal. (C) The effect of different power illumination on the phase transition at room temperature. By recording the impact of different intensities of terahertz light irradiation on the bias phase transition point at room temperature. It can be seen that different light intensities have a significant regulatory effect on the position of the phase transition voltage at room temperature. (D) Photocurrent response of the device under different bias voltages with illumination conditions at 0.04 , 0.12 , and 0.30 THz. By applying a electrical field ranging from 0 to 0.32 V/m to the device in sequence, and scanned the terahertz light response current under 0.02-0.04 THz, 0.08-0.12 THz, and 0.24-0.3 THz. (E) Comparison of photoresponse before and after the abrupt change at 0.3 THz. When the electrical field changes from 0 to 0.32 V/m, a significant increase in the response current can be seen. This is mainly due to the charge density wave phase transition of the material beginning to occur as the bias voltage increases, which leads to a change in the band structure. At this point, low-energy photons exhibit a significantly enhanced ability to excite carriers due to changes in the energy band. The combined effects of the material structural changes and the enhancement of light-induced capabilities lead to a sudden increase in the photoresponse value.

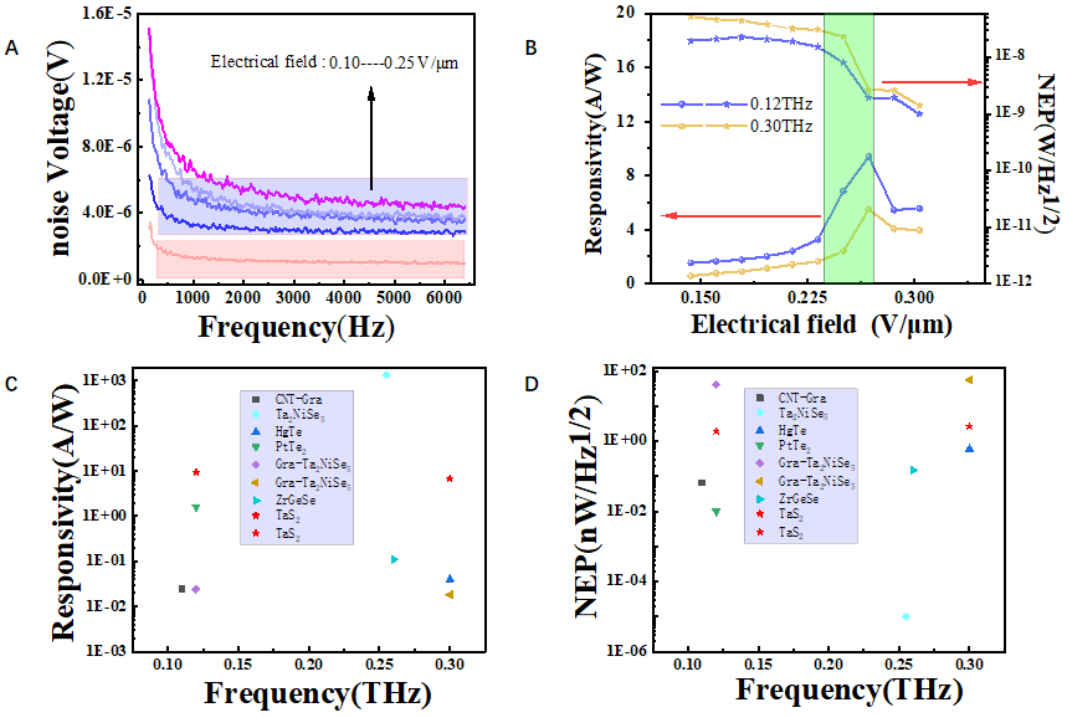

Figure S3. **Noise testing and performance comparison.** (A) Noise spectrum measured under different bias voltages. NEP is defined as the minimum detectable power per unit bandwidth. At low modulation frequencies (less than 1 kHz), the noise current is mainly dominated by flicker noise. In the low frequency range, 1/f noise (flicker noise) dominates the contribution to noise voltage. With the increase in modulation frequency, the contribution of noise voltage decreases exponentially. For frequencies higher than 1 kHz, the noise of the device gradually stabilizes. Therefore, by using noise current with a modulation frequency of 1 kHz to evaluate NEP, the impact of flicker noise can be minimized. At higher frequency, the main noise sources in our detector system consist of v_t and v_b, caused by thermal motion or fluctuations of electron density and the uncorrelated arrival of electrons induced by the applied bias voltage, respectively. The total noise can be calculated by the following formula $v_n = (v_t + v_b)^{1/2} = (4k_BTr + 2qI_dr^2)^{1/2}$, where k_B is the Boltzmann constant, T is the

temperature of the detector, r is the device resistance, and q is the elementary charge.To further explore the performance of this photodetector, we used a dynamic signal analyzer (SR785) to obtain the noise spectrum of the device. (B) Current responsivity and equivalent noise power of the TaS_2 device under different bias voltages. At low modulation frequencies (less than 1 kHz), the noise current is mainly dominated by flicker noise, while it stabilizes for frequencies higher than 1 kHz. To evaluate the noise level and sensitivity of the device, we measured the NEP, which calculation formula is NEP=in*r/Rv, where in is the root mean square (RMS) value of the noise current. It can be seen that at the voltage point where the light response shows a significant surge, the noise anomalously shows a downward trend. We speculate that this is due to the material approaching the phase transition point, causing a sudden change in resistance, which leads to a significant reduction in thermal noise. This figure shows the effect of bias voltage on NEP and current response respectively. It can be seen that the device has the NEP of 2.64 nW/Hz0.5 and the current response rate of 5.49 A/W at 0.3 THz. (C) Comparison of responsivity with the reported typical 2D material THz PDs. (D) Comparison of NEP with the reported typical 2D material THz PDs. By comparing the responsivity and the NEP of our detector with the other PDs[1-6] of recent years, it has been validated that our detector exhibits excellent performance.

Reference

1. Ma, W. et al. Detection of Long Wavelength Photons via Quasi-Two-Dimensional

Ternary Ta 2 NiSe 5. ACS Appl. Electron. Mater. 4, 2979–2986 (2022).

2. He, Y. et al. Carbon-based self-powered terahertz detector with multi-walled carbon nanotubes-graphene heterostructure. Carbon 221, 118886 (2024).

3. Xu, H. et al. PtTe 2 -Based Type-II Dirac Semimetal and Its van der Waals Heterostructure for Sensitive Room Temperature Terahertz Photodetection. Small 15, 1903362 (2019).

4. Zhang, K. et al. Self-driven and ultrasensitive room-temperature terahertz photodetector based on graphene-Ta2NiSe5 van der Waals heterojunction. Infrared Physics & Technology 128, 104474 (2023).

5. Zuo, X. et al. High sensitivity HgTe room temperature terahertz photodetector. APL Photonics 8, 046109 (2023).

6. Zhang, L. et al. Ultrasensitive and Self-Powered Terahertz Detection Driven by Nodal-Line Dirac Fermions and Van der Waals Architecture. Advanced Science 8, 2102088 (2021).

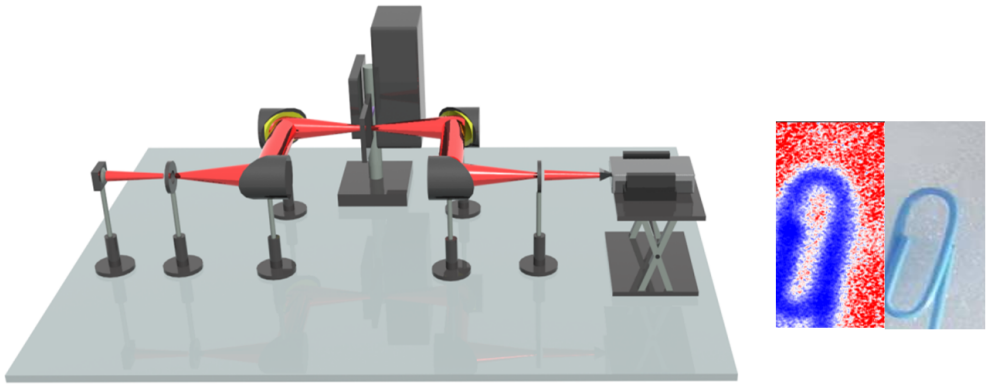

Figure S4. **THz imaging at room temperature.** Schematic of the scanning imaging optical path, along with the optical image and transmission image of the pin under 0.12 THz. The terahertz beam is focused by two off-axis parabolic mirrors to place the imaged object in the focal plane position. Then the terahertz beam is collected and converted into an electrical signal by the detector after being focused by the two off-axis parabolic mirrors. The target object is scanned in the focal plane using a displacement platform, and the electrical signal is collected by a preamplifier and a lock-in amplifier and processed by computer software. The paper clip was used as the test object, with dimensions measuring 15×30 millimeters. The resulting image comprised 150×300 pixels, with an integration time of 20 milliseconds per pixel. The varying shades in the 2D scanned image corresponded to the magnitude of the photocurrent, enabling differentiation of the object's shape based on the variations in photocurrent.

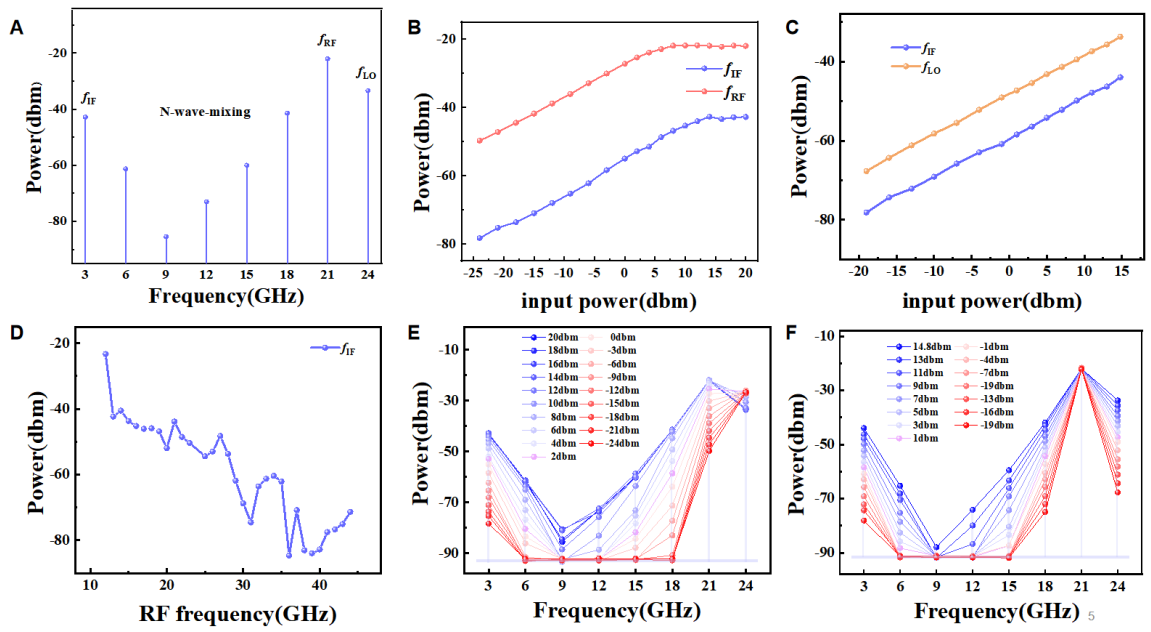

Figure S5. **The optical heterodyne detection experiments under 21 and 24 GHz microwave irradiation.** (A) The corresponding spectrum of the mixing process is shown in the frequency spectrum diagram. Within the range of 0-24 g, we recorded the high-order harmonics as well as the IF signal, RF signal, and LO signal. (B) By changing the power of the RF signal, the corresponding amplitude of the IF signal is obtained. As the RF signal saturates, the IF signal also exhibits saturation. (C) By changing the power of the LO signal, the corresponding amplitude of the IF signal is obtained. Here, the IF signal essentially shows a linear relationship with the LO signal. (D) By changing the RF signal, the corresponding amplitude of the IF signal is obtained. By changing the frequency of the RF signal, the power spectrum corresponding to the IF signal demonstrates a gradually decreasing trend. (E) The spectrum diagram obtained by changing the power of the RF signal. (F) The spectrum diagram obtained by changing the power of the LO signal.

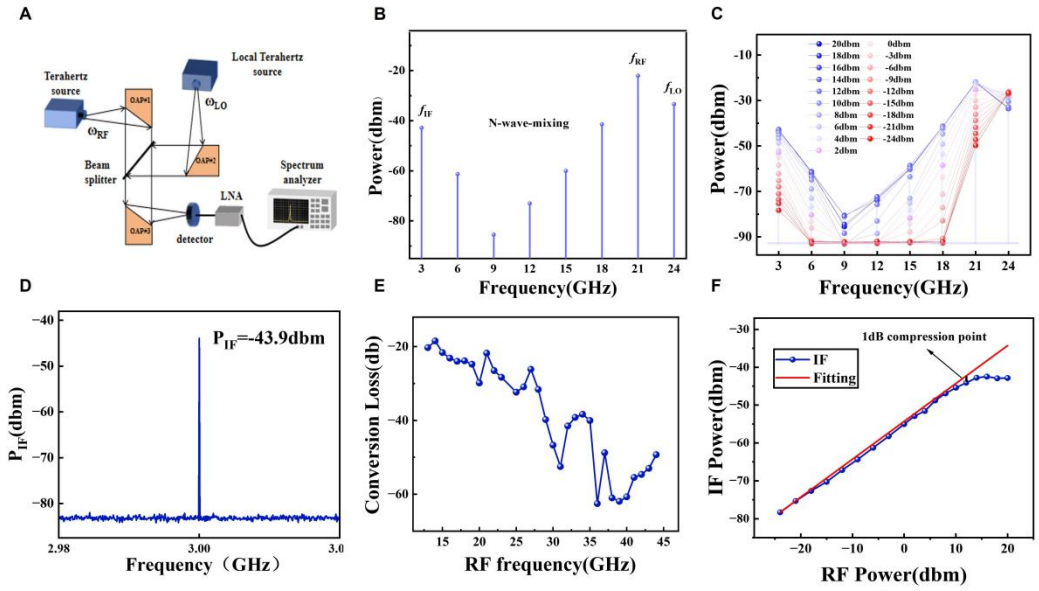

Figure S6: **Schematic and related performance of heterodyne detection.** (A) Diagram of the heterodyne detection link. By conducting heterodyne detection experiments where two electromagnetic waves were simultaneously irradiated onto our terahertz detector. The internal electron oscillations were modulated by both frequencies, resulting in photocurrent components that included higher-order harmonics. Due to the tunable charge density wave (CDW) characteristics of 1T-TaS_2, it exhibited strong nonlinearity at the phase transition point, revealing its potential in the field of heterodyne detection. Here, we present the block diagram of the heterodyne detection link, where two beams of light with different frequencies (radio frequency signal RF and local oscillator signal LO) are incident on the terahertz detector. The device is connected to a low-noise amplifier (LNA), and the intermediate frequency (IF) signal is measured by using a spectrum analyzer. (B) Spectra of Radio frequency signal (RF), Local oscillator signal(LO), Intermediate frequency signal(IF) signals, and higher-order harmonics. when the RF signal is set to 21 GHz and the LO signal to 24 GHz, the IF signal (3 GHz) as well as numerous higher-order harmonic signals (6, 9,

12, etc.) can be obtained. (C) spectrum of the RF signal power variation. When varying the intensity of the RF signal, a concomitant decrease in the intensity of the harmonic signals is observed. This is because the strength of the harmonic signals depends both on the degree of nonlinearity of the device and its response to the RF and LO signals. (D) Spectrum of the IF signal. Figure D shows the measured values when both the RF and LO signals are set to their maximum. Furthermore.(E) Conversion loss with varying RF signal frequency. Figure E illustrates the conversion loss range (18.47 ~ 62.57 dB) corresponding to different RF signal frequencies. (F) 1 dB compression point obtained by varying the power of the RF signal.Figure f displays the 1 dB compression point of the device. By evaluating this performance, we can determine the relationship between output and input signal power, which is crucial for effective system design.

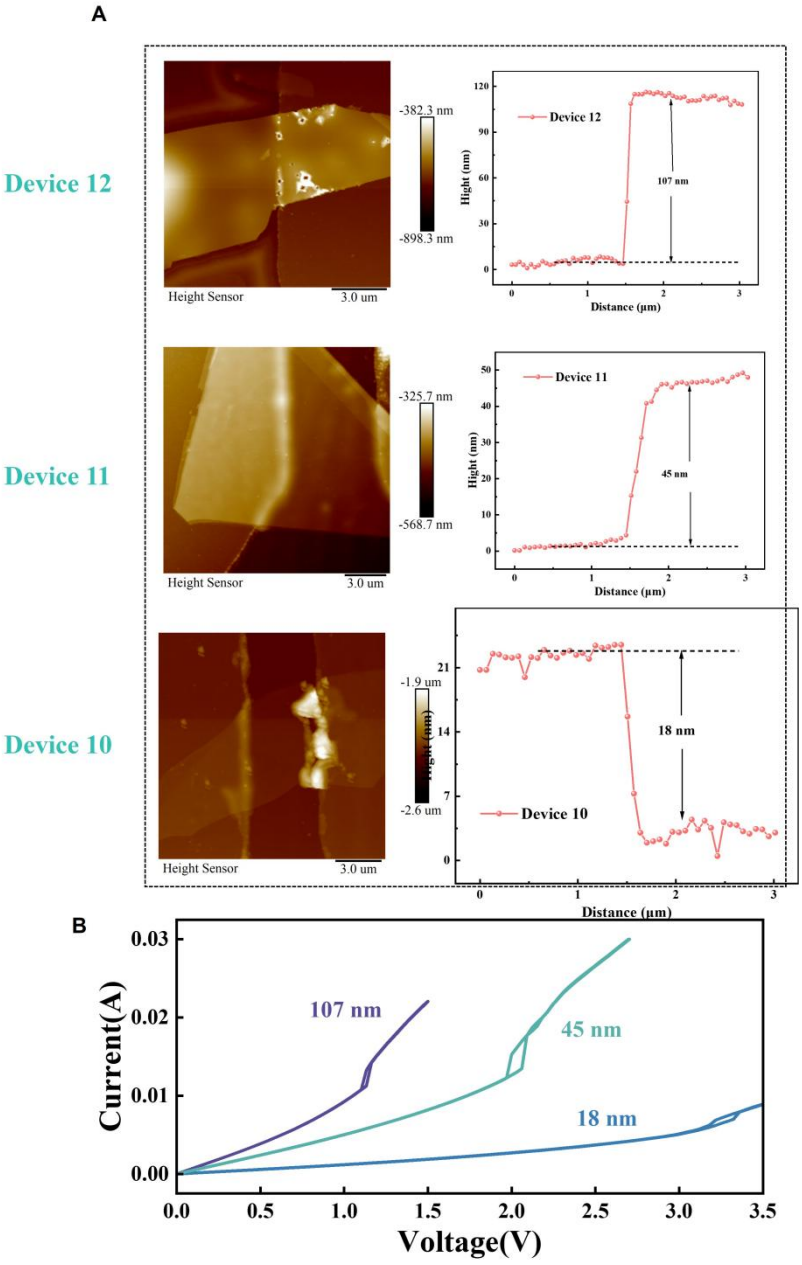

Figure S7: **Thickness-dependent I-V characteristics of TaS_2.** (A) AFM for there devices of different thickness. (B) Hysteresis I-V characteristics. Figure S7 presents thickness-dependent I-V characteristics of TaS_2 devices measured at room temperature. The measurements reveal several notable trends as sample thickness decreases from 107 nm to 18 nm. First, the threshold voltage for phase transition shifts toward higher values in thinner samples, indicating increased stability of the initial phase against field-induced transitions. This behavior is consistent with dimensional confinement effects

observed in other layered CDW materials. The hysteresis window between forward and reverse sweeps also exhibits thickness dependence. The 107 nm sample shows a relatively narrow hysteresis, whereas the 45 nm sample displays a more pronounced hysteretic behavior. Interestingly, the 18 nm sample exhibits a distinct I-V profile with a significantly reduced current magnitude and altered transition characteristics. This thickness-dependent hysteresis likely reflects modifications in the energy landscape between competing phases as dimensionality is reduced.

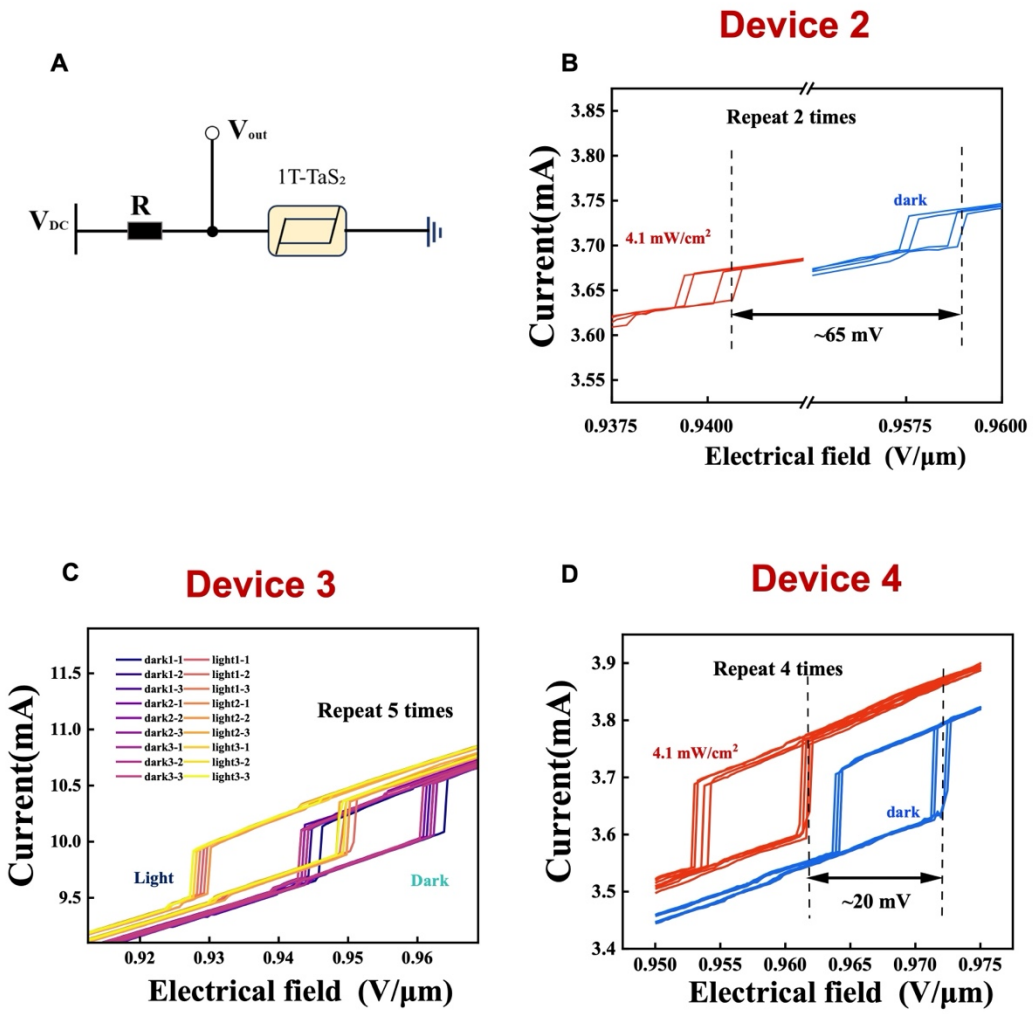

Figure S8: **Verify device repeatability.** (A) Measurement of device phase transition using series resistance. The phase change phenomenon can be altered by connecting resistors in series. (B) Hysteresis IV curves under light and dark conditions with the 500Ω series resistance. (C) Hysteresis IV curves under light and dark conditions without the 500Ω series resistance. It was observed that the difference between the phase change voltage and the hysteresis voltage increased from 20mV to 65mV after connecting resistors in series. (D) Repetition of hysteresis IV curves.This process was repeated for four rounds, with each round consisting of three repetitions, verifying the reproducibility of the device's phase change hysteresis phenomenon.

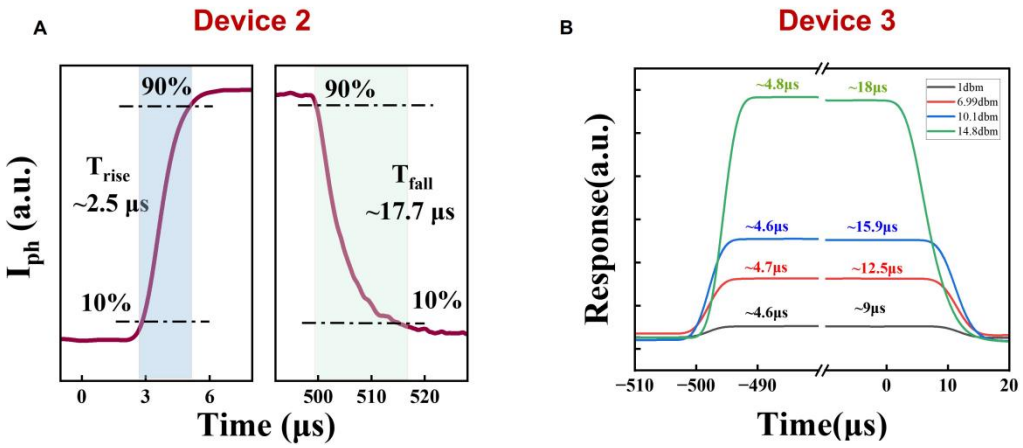

Figure S9. **Device Response Time.** (A) Rise time and fall time. The relatively short rise timesuggests efficient coupling between the incoming THz radiation and the lattice, allowing for rapid generation of photocurrent. In contrast, the fall time (τ fall $\approx$ 17.7 μs)is influenced by the relaxation dynamics of the lattice and the time required for thesystem to return to its initial CDW state. The relatively longer fall time could be attributed to the stabilization of the CDW phase and the slower recombination of photo-excited carriers. (B) Rise time and fall time at different power levels. Figure B verified the relationship between rise time and fall time under different power levels. It can be observed that the rise time does not exhibit a significant linear relationship with power, while the fall time demonstrates a clear power dependence.revealing the asymmetric dynamics between CDW excitation and relaxation.

A

A → C			
Light density	V_{ds}	Last	Out
0	0	0	0
0	1	0	0
0	0	1	0
0	1	1	0
1	0	0	0
1	1	0	0
1	0	1	0
1	1	1	1

B

A → F			
Light density	V_{ds}	Last	Out
0	0	0	0
0	1	0	0
0	0	1	0
0	1	1	1
1	0	0	0
1	1	0	1
1	0	1	0
1	1	1	1

C

A → G			
Light density	V_{ds}	Last	Out
0	0	0	0
0	1	0	1
0	0	1	0
0	1	1	1
1	0	0	0
1	1	0	1
1	0	1	0
1	1	1	1

D

A → D			
Light density	V_{ds}	Last	Out
0	0	0	0
0	1	0	0
0	0	1	0
0	1	1	1
1	0	0	0
1	1	0	0
1	0	1	0
1	1	1	1

E

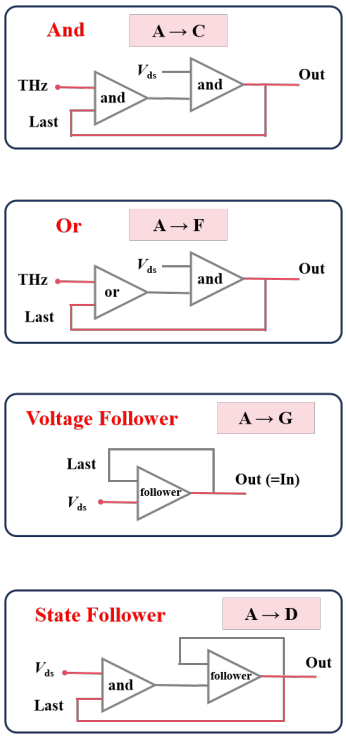

Figure S10. **Demonstration of non-volatile basic optoelectronic logic functions of TaS_2 device.** Truth table of the device implementing logic functions at different intensity pulse voltages (light intensity "0" for the dark, "1" for a terahertz wave with a light intensity of 2.1 mW/cm^2 , V_{ds} for the applied bias voltage, and Last and Out for the CDW phase state in which the device is in). (A) And gate; (B) Or gate; (C) Voltage follower; (D) State follower; (E) Schematic diagram of the implemented logic function corresponding to the above figure one by one.